

Electrochemical Lattice Engineering of Bismuthene for Selective Glycine Synthesis

Sijia Liu, Guanzheng Wu, Jiadi Jiang, Yidong Yang, Aijun Du, Wuyong Zhang, Xin Mao,* Lei Dai,* and Qing Qin*

Glycine plays a crucial role in various industrial and daily applications. However, traditional synthesis methods are often associated with high toxicity, energy intensity, and inefficiency. This study introduces an efficient and eco-friendly method for synthesizing glycine via the reductive coupling of oxalic acid and nitrate using a Bi metal catalyst, enhanced by lattice strain from Bi and oxide composites undergoing electrochemical transformation. At an applied potential of -0.76 V versus the reversible hydrogen electrode (RHE), the Bi catalyst achieves an impressive glycine Faradaic efficiency (FE) of 79.1%, yielding a record concentration of 0.17 M, substantially higher than conventional Bi-based systems. Furthermore, the introduction of glycolaldehyde and hydroxylamine as reactants raise the glycine FE to 91.3% with a production rate of $2433.3 \mu\text{mol h}^{-1}$ under identical conditions. Electrochemical analysis and theoretical calculations demonstrate that lattice expansion notably boosts glycine synthesis by facilitating NH_2OH formation and promoting the efficient reduction of oxime intermediates. These results underscore the significance of lattice engineering in enhancing active site performance and accelerating reaction kinetics, offering a sustainable and efficient alternative to traditional glycine synthesis methods.

meat production, and the chemical industry.^[1] Traditional industrial synthesis of glycine still predominantly relies on the Strecker synthesis, which involves aldehyde, ammonia, and cyanide.^[2] Enzymatic and microbial fermentation methods, while more environmentally benign, are generally time-consuming and energy-demanding.^[3] As a result, electrochemical reforming of C and N precursors under ambient conditions offers a promising and green alternative for efficient C–N bond formation in glycine synthesis.^[4] Oxalic acid (OA), a highly active electrochemical reagent, is particularly attractive as it can be produced from CO_2 electroreduction or biomass conversion, serving as a renewable carbon precursor for amino acid synthesis.^[5] On the N side, nitrate (NO_3^-), with its higher polarity and lower N=O bond dissociation energy (204 kJ mol^{-1}) compared with N_2 , exhibits significantly greater reactivity, making it a more suitable N precursor for electrochemical transformations.^[6] Therefore, the co-reduction of OA and

1. Introduction

Glycine, a non-essential amino acid, is crucial in the biosynthesis of proteins and finds extensive applications in pharmaceuticals,

NO_3^- holds substantial promise for glycine synthesis.^[7] However, achieving high performance remains a challenge due to the complex reaction network and the difficulty in steering the reduction pathways toward a single product.^[8]

S. Liu, G. Wu, J. Jiang, Y. Yang, Q. Qin
College of Chemistry and Materials Science
Anhui Normal University
Wuhu 241002, P. R. China
E-mail: qing.qin@ahnu.edu.cn

A. Du, X. Mao
School of Chemistry and Physics and Centre for Material Science
Faculty of Science
Queensland University of Technology
Gardens Point Campus, Brisbane, QLD 4001, Australia
E-mail: xin.mao@adelaide.edu.au

W. Zhang
Zhejiang Key Laboratory of Advanced Fuel Cells and Electrolyzers Technology
Ningbo Institute of Materials Technology and Engineering
Chinese Academy of Sciences
Ningbo, Zhejiang 315201, P. R. China

L. Dai
Key Laboratory for Special Functional Materials of Ministry of Education
School of Materials Science and Engineering
Academy for Advanced Interdisciplinary Studies
Henan University
Kaifeng 475004, P. R. China
E-mail: dailei@henu.edu.cn

Q. Qin
Key Laboratory of Advanced Energy Materials Chemistry (Ministry of Education)
Nankai University
Tianjin 300071, P. R. China

The ORCID identification number(s) for the author(s) of this article can be found under <https://doi.org/10.1002/adma.202500843>

DOI: 10.1002/adma.202500843

Previous studies have demonstrated that lattice strain can alter the interatomic distances in catalysts, thereby modulating both the surface geometry and electronic structure.^[9] Unlike traditional methods of material modification, such as doping, defect engineering, and ligand modification, strain engineering offers a more straightforward and controllable approach without the need to introduce foreign atoms.^[10] This is particularly advantageous, as the incorporation of a secondary component may unintentionally enhance competing reactions, such as the hydrogen evolution reaction (HER), thereby reducing the efficiency toward the desired product.^[11] Furthermore, d-band theory has elucidated the impact of strain on the binding energy of chemical intermediates, reinforcing the concept that lattice strain can serve as a powerful tool for optimizing catalytic performance.^[12] Indeed, numerous studies have reported that tuning local tensile strain can boost the catalytic performance in CO₂ reduction.^[13] However, the influence of lattice strain on the selectivity of C–N coupling for glycine synthesis has received far less attention. The broader and intrinsic correlations between lattice strain and glycine synthesis with 12-electron-pathway remain poorly understood, which is compounded by the well-established complex linear scaling relationships among reaction intermediates.^[14] Consequently, it is of great interest to investigate how tensile strain affects the co-reduction of OA and NO₃[−]. Recent advances have introduced various strategies to induce lattice strain, including second-metal doping, core-shell structure fabrication, support effects, and crystal engineering.^[15] However, the complexity of these catalyst designs often hinders their large-scale production and the systematic establishment of structure-activity relationships. Therefore, exploring simplified and efficient methods to induce lattice strain while maintaining high catalytic performance remains a critical area of research.

In C–N coupling reactions, hydroxylamine (NH₂ OH) is recognized as a crucial nucleophilic intermediate, which attacks the carbon center to form oxime.^[8] Consequently, it is hypothesized that Bi-based materials, known for their favorable performance in the nitrate reduction reaction (NITRR) for NH₂ OH production, could enhance the co-reduction of OA/NO₃[−] for efficient glycine synthesis.^[16] In this study, we report the synthesis of single-component Bi metal with induced lattice strain through an in-situ electrochemical transformation of Bi-based composites, confirmed via in-situ Raman spectroscopy. The resulting Bi electrode exhibits a maximum FE for glycine of 79.1% at a potential of −0.76 V versus the reversible hydrogen electrode (RHE), achieving an unprecedented glycine concentration of 0.17 M. Moreover, the induced lattice strain significantly improved the selectivity of both NITRR and the oxalic acid reduction reaction (OARR), yielding higher FE for NH₂ OH and glyoxylic acid (GX), respectively, compared to conventional Bi metal. Electrochemical analysis and Fourier-transform infrared (FT-IR) spectroscopy identified enhanced formation toward NH₂ OH and glyoxylic acid oxime (GAO) as key intermediates in the glycine synthesis pathway. To gain further insight into the reaction mechanism, theoretical calculations were performed. These calculations reveal the reduced free energy barriers for NH₂ OH formation and the subsequent reduction of GAO, providing a comprehensive understanding of the enhanced reaction kinetics driven by lattice strain.

2. Results and Discussion

The Bi electrode was synthesized at room temperature facilitated by sodium borohydride as a reducing agent. High-resolution transmission electron microscopy (HRTEM) reveals the presence of small nanodots distributed within nanosheets with an average size of around 5 nm (Figure 1a). The interplanar spacings of 0.35 and 0.33 nm are assigned to the Bi₂O₃ (022) and Bi (012), respectively (referred to as Bi₂O₃-Bi, Figures 1b). X-ray diffraction (XRD) analysis identifies peaks corresponding to hexagonal Bi (JCPDS No. 41–1246, Figure 1c), while the absence of detectable Bi₂O₃ peaks is likely due to the high dispersion and nanoscopic size of the oxide domains. X-ray photoelectron spectroscopy (XPS) of the Bi₂O₃-Bi exhibits characteristic peaks at 162.2 and 156.9 eV, attributed to the Bi⁰ species (4f_{5/2} and 4f_{7/2}, Figure S1, Supporting Information).^[17] Additional peaks at 164.2 and 158.9 eV are assigned to bismuth oxides, suggesting possible structural dynamics during redox processes.^[18] To further investigate the structural evolution, Bi₂O₃-Bi was activated in OA/NO₃[−] electrolyte under co-reduction conditions (Figure S2, Supporting Information). The final reduced sample, denoted as e-Bi, exhibits a consistent lattice spacing of 0.34 nm (012) for metallic Bi, as shown by high-angle annular dark field scanning transmission electron microscopy (HAADF-STEM, Figure 1d,e), reflecting a lattice expansion relative to the Bi₂O₃-Bi precursor. The XRD pattern (Figure 1c) for e-Bi also shows a slight shift toward lower angles compared to Bi₂O₃-Bi, indicating lattice expansion due to strain. Such strain effect was further quantified through p-band center calculations (Figure 1f; Figure S3, Supporting Information), revealing an upward shift toward the Fermi level (from −1.42 to −1.23 eV) with increasing tensile strain. Compared to commercial Bi nanoparticles (c-Bi, Figure S4, Supporting Information), this modification could enhance the adsorption of key intermediates, promoting more efficient electrocatalytic performance.^[19] Furthermore, in-situ Raman spectroscopy was performed under various potentials (Figure S5, Supporting Information) to investigate the transformation process. The spectra reveal characteristic peaks at 70.5 and 97.0 cm^{−1}, corresponding to the E_g and A_{1g} stretching modes of the metallic Bi–Bi bond, respectively.^[20] Additionally, a peak at 85 cm^{−1} is assigned to the Bi–O bond. As the applied potential became more negative, the intensity of the Bi–O peak gradually diminished and completely vanished at −0.76 V versus RHE, indicating the reduction of Bi₂O₃.^[21] A time-resolved Raman experiment further confirms this transformation, showing that Bi–O bonds disappeared within 600 s (Figure 1g). Thus, the mechanism for the structural transformation from Bi₂O₃-Bi to e-Bi was deduced as follows. Under negative potential, Bi³⁺ ions in Bi₂O₃ are progressively reduced to metallic Bi⁰. This reduction process is accompanied by the removal of oxygen atoms from the lattice, likely in the form of OH[−] or water, leading to the collapse of the original Bi₂O₃ structure. As oxygen atoms are eliminated, the lattice undergoes reorganization, with metallic Bi⁰ atoms forming new crystalline domains. During this reorganization, tensile strain develops within the lattice, expanding the interplanar spacing. This expanded lattice structure in e-Bi is thermodynamically more stable than the original Bi₂O₃-Bi. Additionally, the upward shift of the p-band center toward the Fermi level in e-Bi reduces the

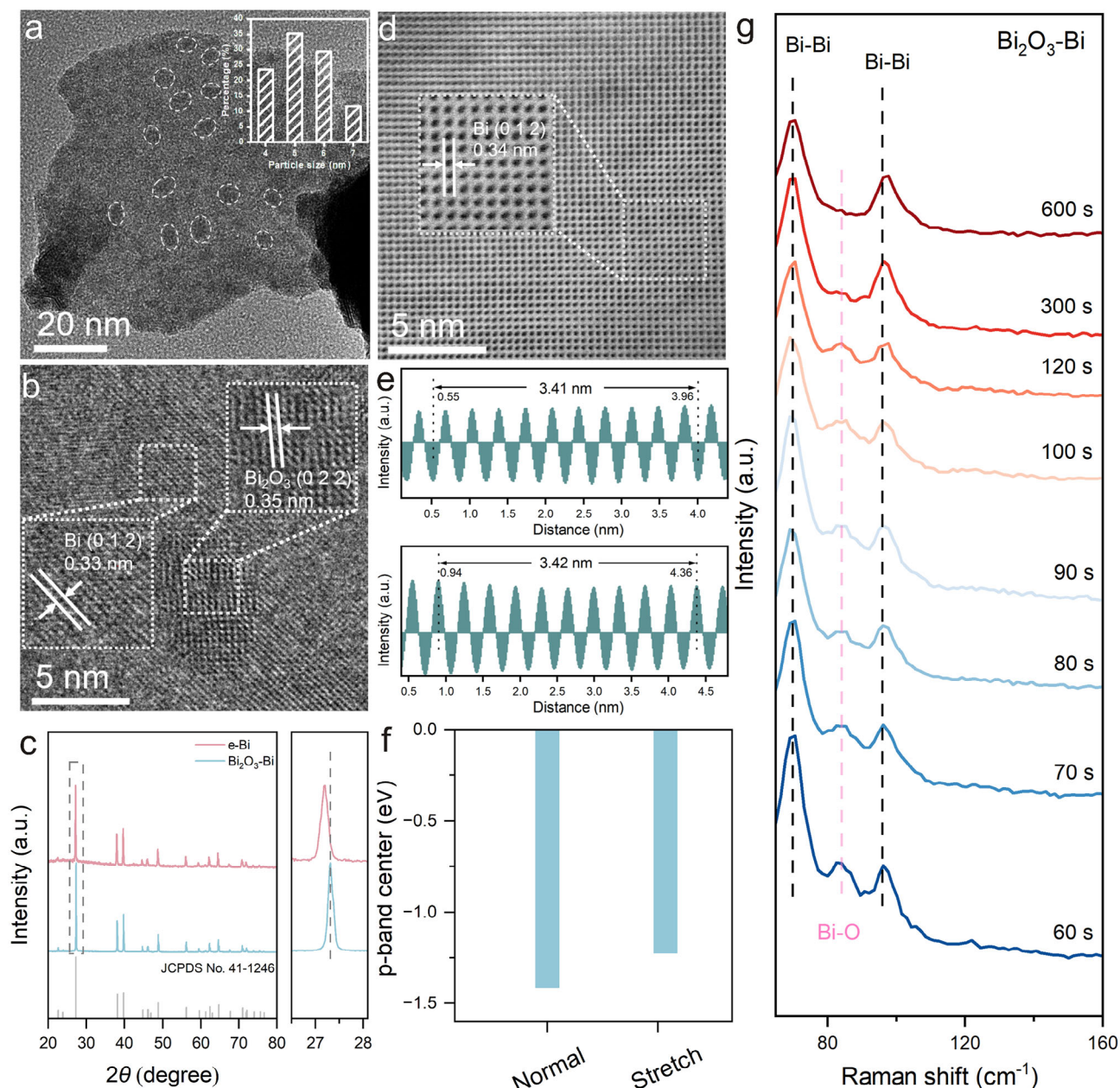


Figure 1. a) TEM image of $\text{Bi}_2\text{O}_3\text{-Bi}$ (the inset: particle size distribution). b) The spherical-aberration correction electron microscopy image with the corresponding crystal lattice of Bi_2O_3 and Bi. c) XRD patterns. d) The spherical-aberration correction electron microscopy image with the corresponding crystal lattice of e-Bi. e) Line profile of e-Bi. f) Calculated p-band centers and adsorption energies at e-Bi. g) In situ Raman spectra acquired during the electroreduction of $\text{Bi}_2\text{O}_3\text{-Bi}$.

energy barrier for the adsorption of reactants and intermediates, enhancing its electrocatalytic performance.

The electrocatalytic activity of e-Bi and c-Bi electrodes for the co-reduction of OA and NO_3^- was thus evaluated in an H-cell. Linear sweep voltammetry (LSV) curves (Figure S6, Supporting Information) were recorded for individual and combined electrolytes: OA, NaNO_3 , and OA/ NaNO_3 . The co-reduction of OA/ NO_3^- exhibits a more positive onset potential and higher current density compared to individual OARR and NITRR, indicating the possible enhanced C–N coupling on the e-Bi

electrode.^[22] The reaction products were further analyzed using proton nuclear magnetic resonance ($^1\text{H-NMR}$, Figures S7–S9, Supporting Information), ultraviolet-visible (UV-vis) absorption spectroscopy (Figures S10–S12, Supporting Information), and gas chromatography after the chronoamperometry tests (Figure S13, Supporting Information). A volcano-shaped relationship between FE and applied potential was observed for glycine, with an FE exceeding 50% across a broad potential range (–0.46 to 1.06 V vs RHE, Figure 2a). The highest FE of 79.1% was achieved at –0.76 V versus RHE, corresponding to a partial

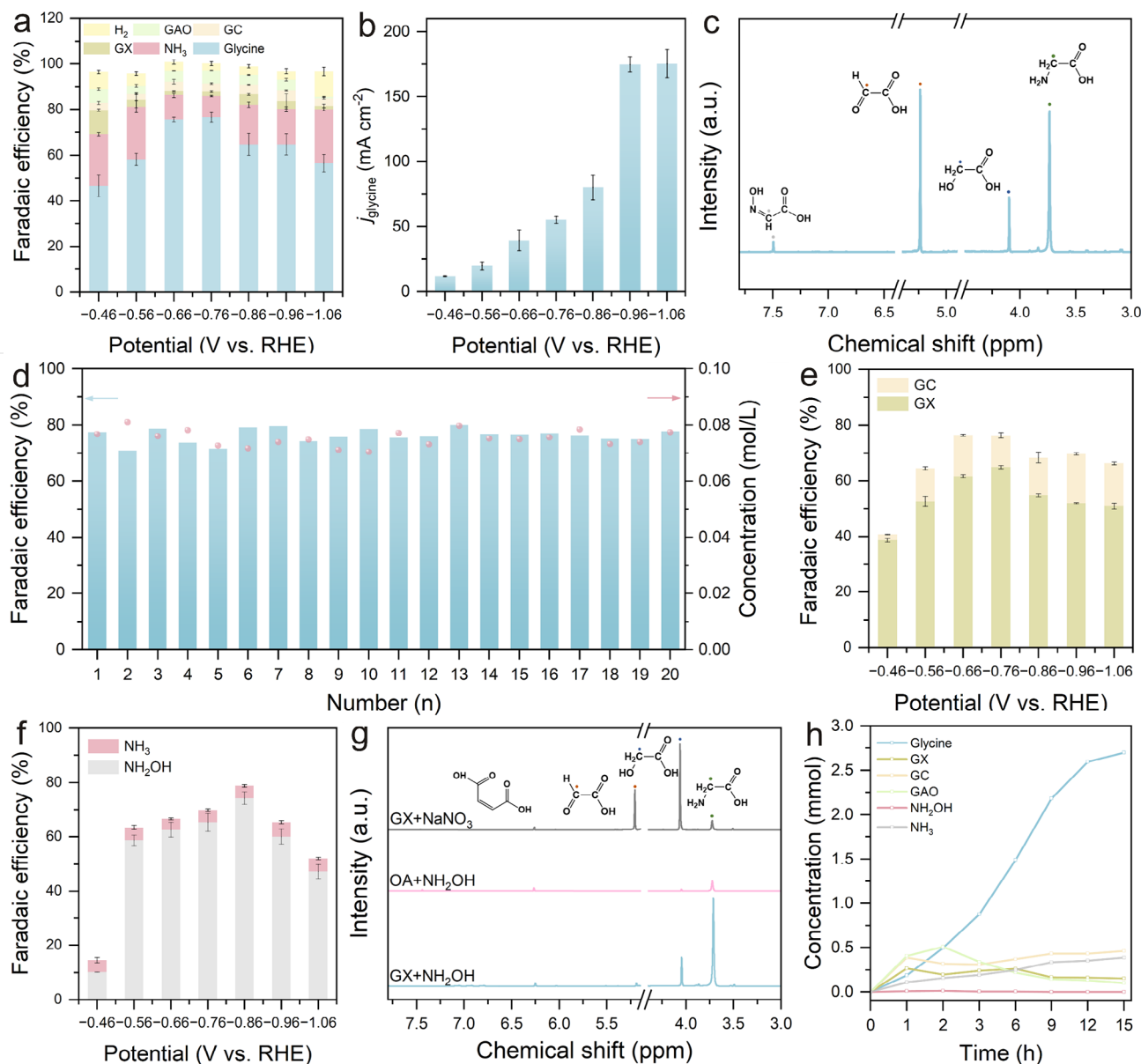


Figure 2. a) FE in 0.5 M OA + 0.5 M NaNO₃ for e-Bi with different potentials. b) Partial current density of glycine with different potentials. c) ¹H-NMR spectra of different products. d) FE and glycine concentration in 0.5 M OA + 0.5 M NaNO₃ within the 20-cycle tests at the potential of −0.76 V versus RHE. e) FE of GX and GC in 0.5 M OA. f) FE of NH₂OH and NH₃ in 0.5 M NaNO₃. g) ¹H-NMR spectra of different products in various electrolyte conditions. h) Time-tracking of concentration of different products at the potential of −0.76 V versus RHE in 0.5 M OA + 0.5 M NaNO₃.

current density of 56.9 mA cm^{−2} (Figure 2b). Additional products, including GX, glycolic acid (GC), GAO, ammonia (NH₃), and hydrogen (H₂), were also detected (Figure 2c; Figure S14, Supporting Information). Notably, the maximum concentration of glycine reached 0.17 mol L^{−1} at −1.06 V versus RHE with a remarkable current density of 183.0 mA cm^{−2} (Figure S15, Supporting Information). In addition, e-Bi electrode also exhibits a desirable glycine selectivity in the co-reduction of OA and NO₃[−] (Figures S16, Supporting Information). Beyond the impressive catalytic activity, e-Bi demonstrates excellent durability, maintaining its structural integrity and morphology throughout multiple cycles (Figure 2d; Figure S17, Supporting Information). XRD and

TEM analyses (Figure S18, Supporting Information) confirm the preservation of the electrode's structure after electrocatalysis.

Individual OARR and NITRR reactions were carried out using the e-Bi electrode in 0.5 M OA and 0.5 M NaNO₃, respectively (Figure S19, Supporting Information), to gain deeper insight into the C–N coupling mechanism. NITRR predominantly yields NH₃ and NH₂OH, with NH₂OH achieving a maximum FE of 75.9% at −0.86 V versus RHE, consistently outcompeting NH₃ production (Figure 2e). For OARR, GX and GC emerge as the key products, with GX showing a notably higher FE than GC (Figure 2f). When OA or NO₃[−] was replaced by GX or NH₂OH, respectively, the co-reduction of GX/NO₃[−] and OA/NH₂OH

effectively produced glycine (Figure 2g). This aligns with the electrophilic behavior of GX and the nucleophilic nature of NH_2OH . As proof, a mixture of 10 mM GX and 5 mM NH_2OH at room temperature rapidly yielded GAO through C–N coupling (Figure S20, Supporting Information), leaving minimal NH_2OH unreacted (Figure S21, Supporting Information).^[8] Similarly, electrocatalytic co-reduction of GX and NH_2OH over e-Bi at -0.76 V versus RHE confirms the formation of glycine and GAO, establishing GAO as a crucial intermediate for glycine synthesis. The rapid conversion of GAO contributes to a high glycine FE of 91.3% with a production rate of $2433.3 \mu\text{mol h}^{-1}$ (Figure 2g). Moreover, the product concentrations were tracked throughout long-term electrolysis (Figure 2 h; Figure S22, Supporting Information). During the initial hour, GX and GAO accumulated rapidly, reflecting OARR's higher activity compared to NITRR, as indicated by the more positive onset potential in the LSV curves (Figure S6, Supporting Information). With OARR proceeding efficiently, most NH_2OH was swiftly consumed by GX, leaving only trace amounts detectable. GX levels, however, remained steady, suggesting that maintaining excess GX is critical for high selectivity in C–N coupling. After two hours, GAO levels began to stabilize while glycine concentrations increased, indicating a steady conversion of GAO into glycine. Meanwhile, partial reductions of GX and NH_2OH led to the formation of GC and NH_3 as byproducts.

Highlighting the unique structure of e-Bi, c-Bi was also tested as an electrode for glycine synthesis (Figure S23, Supporting Information). While both electrodes exhibit a similar volcano-shaped FE profile, the FE for glycine was consistently lower across the potential range for c-Bi. At -0.76 V versus RHE, the maximum FE for glycine achieved with c-Bi was only 54.1%, significantly lower than the 79.1% observed with e-Bi. Additionally, c-Bi produces higher proportions of H_2 and GC as byproducts. Further investigation into the individual reduction of OA and NO_3^- (Figure S24, Supporting Information) reveals that c-Bi enhanced GC formation, reaching a maximum FE of 43.3%, approximately 2.5 times that of e-Bi, suggesting an increased tendency for GX further reduction on c-Bi. Besides, NH_2OH production from NITRR is less favorable on c-Bi. Electrochemical in-situ Raman analysis (Figure S25, Supporting Information) confirmed the persistence of Bi–Bi bonds throughout the reaction, demonstrating the structural stability of c-Bi. Furthermore, in-situ electrochemical impedance spectroscopy (EIS) measurements were conducted to investigate the catalytic kinetics and the electrode/electrolyte interface properties under varying potentials. In the $\text{OA} + \text{NO}_3^-$ electrolyte, the Bode plots of both e-Bi and c-Bi (Figure 3a; Figure S26, Supporting Information) exhibit characteristic peaks in the low-frequency region (<100 Hz), in which the values of e-Bi are consistently smaller than those of c-Bi, indicating that more charge is stored at the electrolyte/electrode interface and participates in the Faradaic reaction.^[23] Moreover, compared to c-Bi, the peak position of e-Bi shifts to the lower frequency region, confirming the effective suppression of the Heyrovsky step on e-Bi.^[24] It can thus prevent hydrogen evolution, as evidenced by the lower H_2 FE (Figure 2b; Figure S23b, Supporting Information). Besides, electron transfer resistance is also reduced on e-Bi, exhibiting a smaller semicircle compared to c-Bi (Figure 3b). Overall, these comparative results underscore the formation of unique active sites on e-Bi during the in-situ trans-

formation of $\text{Bi}_2\text{O}_3\text{-Bi}$. The structural differences between c-Bi and e-Bi suggest that the lattice expansion observed in e-Bi plays a crucial role in facilitating the co-reduction of OA and NO_3^- , promoting glycine synthesis with higher efficiency.

To further elucidate the C–N coupling mechanism on e-Bi, we employed in-situ Fourier-transform infrared spectroscopy (FTIR) (Figure 3c,d) to monitor the co-reduction process of OA and NO_3^- , aiming to comprehensively map out the reaction pathway and intermediate evolution. The peaks at 1778 and 1326 cm^{-1} are attributed to the adsorption of OA and NO_3^- , respectively.^[25] Besides, the characteristic peak at 1198 cm^{-1} associated with the intermediate configuration of $^*\text{NH}_2\text{OH}$ is closely related to the transition.^[8] Comparing e-Bi and c-Bi (Figure 3e,f) catalysts, it is evident that the signal intensity of e-Bi increases progressively as the potential becomes more negative, while this phenomenon is not as pronounced for c-Bi. This suggests that Bi with enlarged lattice structures has a stronger ability to convert NO_3^- into NH_2OH , which is consistent with the experimental results. Similarly, the downward adsorption peak at 1419 cm^{-1} is assigned to the formation of GX. The difference in peak intensity elucidates that the GX generated on e-Bi is rapidly captured by the larger amount of NH_2OH , resulting in a weaker signal trend.^[26] The peaks at 1682 and 1583 cm^{-1} correspond to the C=N stretching vibration mode of glyoxylic acid oxime and the C–N vibration mode of glycine, respectively, indicating the effective occurrence of C–N coupling.^[27] Based on the preceding discussions, the proposed mechanism (Figure S27, Supporting Information) involves the reduction of OA and NO_3^- to GX and NH_2OH , respectively. Subsequently, NH_2OH acts as a nucleophile, attacking GX to form GAO, which undergoes further reduction to yield glycine. The structural transformation from $\text{Bi}_2\text{O}_3\text{-Bi}$ to e-Bi plays a pivotal role by not only accelerating the production of GX and NH_2OH but also inhibiting their over-reduction. Additionally, the e-Bi electrode facilitates the efficient conversion of GAO into glycine, ensuring high selectivity for the desired product.

Therefore, DFT calculations were performed on two Bi models representing e-Bi and c-Bi, each with distinct crystal lattice structures, to explore lattice expansion effect on glycine synthesis. The NO_3^- reduction pathway leading to NH_2OH formation was compared (Figure 4a,b), as NH_2OH , a nucleophilic reagent, plays a critical role by attacking GX to form the GAO intermediate. Initial NO_3^- adsorption is exothermic on both e-Bi and c-Bi, followed by the formation of $^*\text{NO}_2$, an essential intermediate. The subsequent hydrogenation step from $^*\text{NO}_2$ to $^*\text{NO}$ is identified as the rate-determining step (RDS), with energy barriers of $+0.454$ eV for c-Bi and $+0.337$ eV for e-Bi, indicating more favorable NITRR on e-Bi. Further hydrogenation steps lead to NH_2OH formation, where the transition from $^*\text{NO}$ to $^*\text{NHO}$ is endothermic on c-Bi, while all other steps are exothermic. The overall process shows NH_2OH formation to be energetically favorable on e-Bi, aligning with experimental results. NH_2OH subsequently reacts with GX to yield GAO (HOOCCHNOH) (Figure 4c,d). The adsorption and reduction of HOOCCHNOH are exothermic on both electrodes until the $^*\text{HOOCCHNH}$ to $^*\text{HOOCCH}_2\text{NH}$ hydrogenation step. On c-Bi, this step requires an energy increase of 0.35 eV, also serving as the RDS for GAO reduction. In contrast, e-Bi requires only an increase of 0.01 eV, indicating superior thermodynamic favorability. Desorption of $^*\text{HOOCCH}_2\text{NH}_2$ from the catalyst surface was endothermic on both electrodes, with energy demands

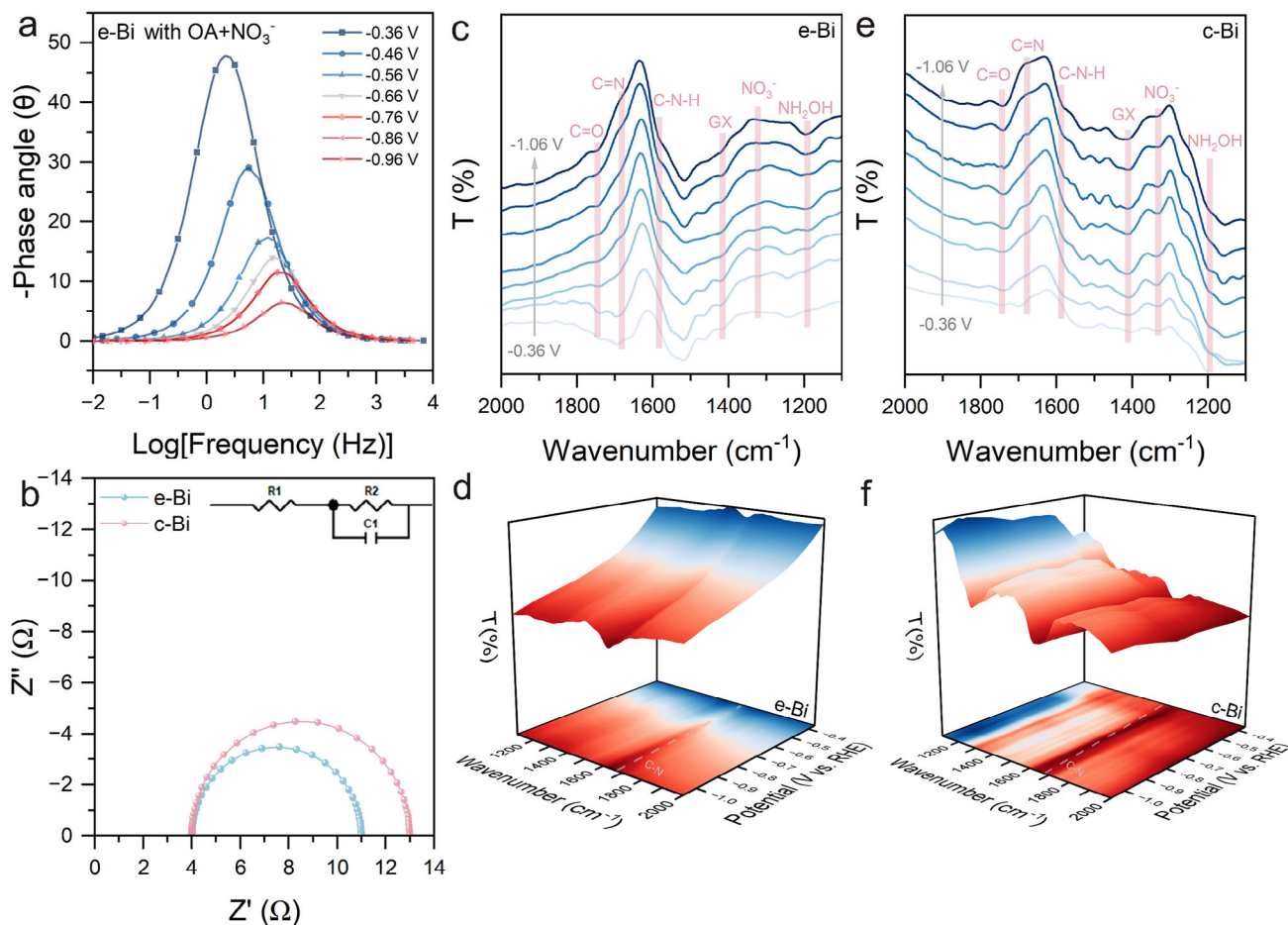


Figure 3. a) Bode phase plots of e-Bi at different potentials in the electrolyte of 0.5 M OA + 0.5 M NaNO₃. b) Nyquist plots of e-Bi and c-Bi in electrolyte of 0.5 M OA + 0.5 M NaNO₃. In situ FTIR spectra during the co-reduction of OA + NaNO₃ of c) e-Bi and e) c-Bi. Three-dimensional FTIR spectra during the co-reduction of OA + NaNO₃ of d) e-Bi and f) c-Bi.

of +0.212 eV for e-Bi and +0.141 eV for c-Bi, also marking the RDS for e-Bi. However, the lower energy barrier in the whole process confirms enhanced performance on e-Bi. These theoretical calculations demonstrate that the expanded lattice structure of e-Bi plays a pivotal role in enhancing glycine synthesis by reduc-

ing energy barriers associated with NH₂OH formation and GAO reduction.

Given the unique structure of e-Bi, we explored the possibility of extending substrate versatility to synthesize other amino acids using this method. Various α -keto acids (pyruvic acid,

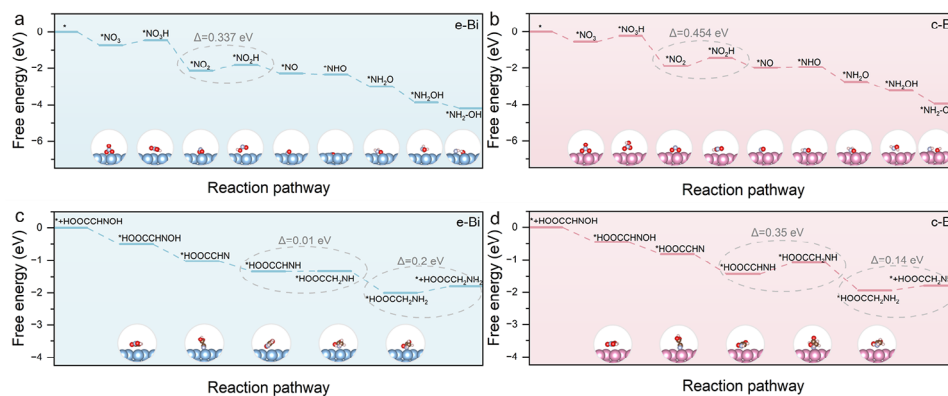
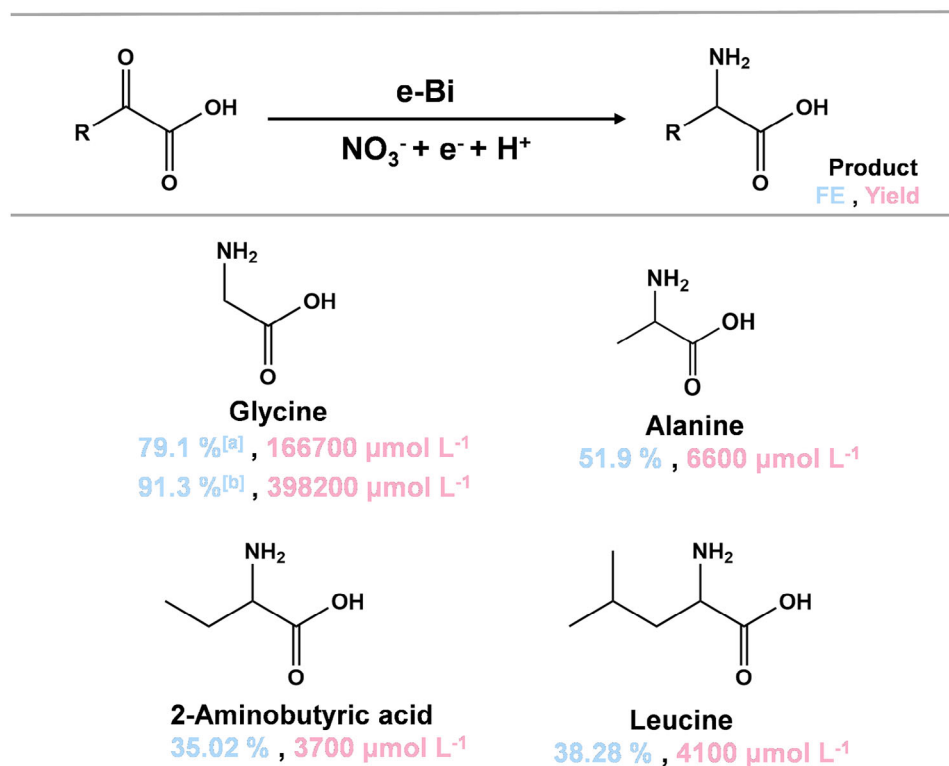


Figure 4. The free-energy diagram for the NO₃[−] reduction pathway on the surface of a) e-Bi and b) c-Bi. The free-energy diagram for the GAO reduction pathway on the surface of c) e-Bi and d) c-Bi.



Scheme 1. The schematic depiction outlines the pathway for the generation of α -amino acids on the e-Bi electrode. Additionally, the molecular structures of the intended amino acid products, along with their corresponding FE and yield rates obtained through electrosynthesis utilizing NO_3^- and diverse α -keto acids (^[a]R = OH; ^[b]R = H), are presented.

2-oxobutyric acid, and 4-methyl-2-oxopentanoic acid) were reacted with NO_3^- over e-Bi to produce the corresponding α -amino acids. The desired products, including alanine, 2-aminobutyric acid, and leucine, were unequivocally confirmed via $^1\text{H-NMR}$ (Figures S28–S30, Supporting Information). The yields and FE were quantified based on their respective standard curves (Figures S31–S33, Supporting Information) and summarized in **Scheme 1**. Notably, e-Bi achieved an FE of 51.9% for alanine, more than three times higher than the 14.6% obtained with c-Bi. Similarly, e-Bi exhibits an impressive FE of 38.3% for leucine production, nearly tenfold higher than the 4.1% of c-Bi. For 2-aminobutyric acid, e-Bi achieved an FE of 35.02%, surpassing the 26.11% of c-Bi. Overall, all tested amino acids (C2–C6) were synthesized with good yields than those obtained with c-Bi. These results demonstrate that the lattice strain strategy we proposed not only enhances catalytic activity but also exhibits excellent universality for the synthesis of diverse amino acids.

3. Conclusion

To conclude, this study highlights the enhanced electrocatalytic performance of e-Bi for glycine synthesis through the co-reduction of OA and NO_3^- . The structural transformation of $\text{Bi}_2\text{O}_3\text{-Bi}$ into e-Bi promotes lattice expansion. The expanded lattice not only stabilizes intermediate states but also promotes selective product formation, demonstrating the potential of lattice-tuned materials for sustainable amino acid synthesis. As a result, e-Bi exhibits superior FE of 79.1% at -0.76 V versus RHE and

enhanced partial current density of 183.0 mA cm^{-2} at -1.06 V versus RHE, compared to commercial Bi. Individual OARR and NITRR demonstrate the e-Bi with enlarged lattice can facilitate NH_2OH and GX formation and inhibit their further individual reduction. DFT calculations and in-situ analysis also confirm that lattice expansion plays a pivotal role in enhancing glycine synthesis by lowering the energy barriers of NH_2OH formation and promoting GAO reduction. The findings highlight the significance of precise lattice engineering to modulate active sites and enhance reaction kinetics, offering a green alternative to conventional chemical synthesis routes.

4. Experimental Section

Chemicals: All the reagents are analytical grade and used without further treatment. Bismuth nitrate pentahydrate ($\text{Bi}(\text{NO}_3)_3 \cdot 5\text{H}_2\text{O}$, AR), sodium borohydride (NaBH_4 , 98%), ethylene glycol ($\text{HOCH}_2\text{CH}_2\text{OH}$, AR) acetone, and sodium carbonate were purchased from Sinopharm Chemical Reagent Co. Ltd. N-(1-naphthyl)-ethylenediamine dihydrochloride, glycine, glyoxylic acid, glycolic acid, sodium hydroxide, salicylic acid, sodium citrate, sodium hypochlorite solution, sulfuric acid, ammonium chloride, trichloroacetic acid, 8-quinolinol, phosphate buffered solution, and ethanol were purchased from Shanghai Macklin Biochemical Co. Ltd. Nafion perfluorinated resin solution (5 wt.% in lower aliphatic alcohols and water) was bought from Sigma Aldrich. Commercial bismuth (Bi, 99.99%, 200 mesh) with a diameter of 100 nm was purchased from Macklin. All chemicals were used as provided without any further purification. Deionized water ($18.2 \text{ M}\Omega\text{-cm}$, Master-515Q, Hitech) was used throughout the experiment.

Synthesis of Bi₂O₃-Bi: 145 mg of Bi (NO₃)₃·5H₂O were dissolved in 20 mL of ethylene glycol under vigorous stirring. Subsequently, 5 mL of 0.05 M aqueous solution of NaBH₄ was introduced into the above mixture at an adding rate of 5 mL per minute with continuous stirring. Once the precipitation process was completed, the resulting product underwent centrifugation, followed by washing with ethanol and deionized water several times. Finally, the product was dried under a vacuum.

Synthesis of e-Bi: In a 0.5 M oxalic acid (OA) + 0.5 M sodium nitrate (NaNO₃) electrolyte solution, Bi₂O₃-Bi electrode was activated at 100 mA cm⁻².

Cathode Preparation: Bi₂O₃-Bi was added into a mixture of 1.96 mL and 40 µL of Nafion solution. After sonicating for 30 min to ensure uniform dispersion, 200 µL of the catalyst ink was evenly dropped onto the carbon paper, and dried naturally, which was then used for electrochemical measurements. During each cycle test, the electrode is gently rinsed with ultrapure water to remove residual electrolytes and loose deposits, then dried with nitrogen purging to prevent water film interference. The electrode is stored under nitrogen protection, while at the same time, cleaning the electrolytic cell and other accessories.

Material Characterizations: Crystal information was gathered through X-ray powder diffraction (XRD) measurements using a SmartLab 9 kW X-ray diffractometer, which employs Cu Kα radiation sourced from a PANalytical X'Pert Pro MPD system (λ = 1.5406 Å). Scanning electron microscope (SEM) was utilized on a Hitachi-S8100 device, operating at an accelerating voltage of 5 kV. For detailed imaging and analysis, a Tecnai G2 20 ST (FEI) instrument was employed at an acceleration voltage of 200 kV to conduct transmission electron microscopy (TEM) and high-resolution TEM (HRTEM). Spherical aberration correction electron microscopy images were captured using Themis Z equipment, which operated at an accelerating voltage of 300 kV. Raman spectroscopy measurements were performed on a Renishaw inVia InSpec micro-Raman spectrometer. Transform Infrared (FT-IR) spectra were recorded using a Bruker Invenio-R instrument. UV-vis spectroscopic measurements were recorded on a UV-6100 spectrometer. Additionally, ¹H-nuclear magnetic resonance (¹H-NMR) spectra were recorded at 400 MHz using Bruker equipment. During electrochemical experiments, the gaseous product was analyzed in real time using an online gas chromatograph (FULI GC9720PULS). The composition and electronic structure of the materials were further analyzed by X-ray photoelectron spectroscopy (XPS) on an AXIS Nova spectrometer (Thermo Alpha), equipped with a monochromatic Al Kα X-ray source (1486.6 eV). The binding energies were calibrated based on the C 1s peak at 284.8 eV.

Electrochemical Measurements: Hg/Hg₂SO₄ was used as the reference electrode, and a Pt sheet served as the counter electrode. A Nafion membrane (117) was applied to separate the H-cell. All potentials were normalized to the RHE (reversible hydrogen electrode) scale according to the formula: E(RHE) = E(Hg/Hg₂SO₄) + 0.656 + 0.059 * pH. Ultrapure water was used as the solvent to eliminate any ionic interference. First, oxalic acid was added to ultrapure water and stirred magnetically at 500 rpm until fully dissolved. Then, sodium nitrate was introduced, and stirring continued for 30 min to ensure complete dissolution. During the electrolysis process, various reduction reactions were conducted under different electrolyte conditions. These included the co-reduction of OA and NO₃⁻, the co-reduction of GX and NH₂OH, as well as the individual reduction of OARR and NO₃⁻. Specifically, electrolysis was performed in 0.5 M OA + 0.5 M NaNO₃ (with 0.5 M OA at the anode), 0.5 M GX + 0.5 M NH₂OH, and 0.5 M OA, along with 0.5 M NaNO₃ + 0.5 M H₂SO₄, respectively.

Linear sweep voltammetry (LSV) curves were collected in different electrolyte solutions at a scan rate of 1 mV s⁻¹. Chronoamperometry tests are conducted at different given potentials under continuous stirring. Electrochemical impedance spectroscopy (EIS) measurements were conducted at open circuit potential within the frequency range of 0.1 MHz to 0.1 Hz, and 80% of resistance compensation was applied. Before all measurements, Ar gas was continuously fed to remove dissolved oxygen from the cathode. A 20-cycle test for glycine synthesis was performed at -0.76 V versus RHE.

NO₂⁻ Detection: A NO₂⁻ color reagent was prepared by adding 50 mL of phosphoric acid, 20 g of p-aminobenzene sulfonamide, and 1 g of N-(1-

naphthyl)-ethylenediamine dihydrochloride into 250 mL of water. During the detection process, 0.1 mL of the color reagent was added to 5 mL of the electrolyte solution, which was then allowed to stand in the dark for 20 min. The absorbance at 540 nm is collected using a UV-vis spectrophotometer.

$$FE_{NO_2^-} = \frac{2 * F * C_{NO_2^-} * V}{46 * Q} \quad (1)$$

where C_{NO₂⁻} is concentration of NO₂⁻ (µg mL⁻¹); F is the Faraday constant; V is the volume of electrolyte solution in the cathodic part; Q is the total amount of charges passing the electrode.

NH₂OH Detection: 1 mL of electrolyte solution, was sequentially mixed with 1 mL of phosphate buffer solution (0.05 M), 0.8 mL of water, 0.2 mL of trichloroacetic acid solution (12 wt.%), and 1 mL of 8-quinolinol solution (1 g of 8-quinolinol dissolved in 100 mL of ethanol), followed by adding 1 mL of sodium carbonate solution (1 M) under vigorous stirring. Then, the mixture was treated in an oil bath at 105 °C for 1 min and cooled down to room temperature. The absorbance at 705 nm was collected using a UV-vis spectrophotometer. The NH₂OH FE was calculated as follows:

$$FE_{NH_2OH} = \frac{6 * F * C_{NH_2OH} * V}{33 * Q} \quad (2)$$

$$n_{NH_2OH} = C_{NH_2OH} * V \quad (3)$$

where C_{NH₂OH} is concentration of NH₂OH (µg mL⁻¹); n_{NH₂OH} is the mass of NH₂OH; F is the Faraday constant; V is the volume of electrolyte solution in the cathodic part; Q is the total amount of charges passing the electrode.

NH₃ Detection: It was achieved using the indophenol blue method. In detail, 5 wt.% salicylic acid and 5 wt.% sodium citrates were added into 200 mL of NaOH solution (1 M) as the color-developing agent. 2 mL of the electrolyte solution was mixed sequentially with 2 mL of the color-developing agent, 1 mL of 0.05 M NaClO solution, and 0.2 mL of 1 wt.% sodium nitroferrocyanide. The absorbance at 654 nm is collected using a UV-vis spectrophotometer. The NH₃ FE was calculated as follows:

$$FE_{NH_3} = \frac{8 * F * C_{NH_3} * V}{17 * Q} \quad (4)$$

$$n_{NH_3} = C_{NH_3} * V \quad (5)$$

where C_{NH₃} is concentration of NH₃ (µg mL⁻¹); n_{NH₃} is the mass of NH₃; F is the Faraday constant; V is the volume of electrolyte solution in the cathodic part; Q is the total amount of charges passing the electrode.

Gaseous products detection: FULI GC9720PULS was applied with a thermal conductivity detector and flame ionization detectors.

FE for H₂ was calculated as follows:

$$FE_{H_2} = \frac{2 * F * n_{H_2}}{Q} \quad (6)$$

where n_{H₂} is the mole of H₂, F is the Faraday constant; Q is the total amount of charges passing the electrode.

¹H-NMR Measurements: 350 µL of electrolyte was mixed with 50 µL of maleic acid and 100 µL of D₂O, followed by analyzing the reaction products using a 400 MHz NMR spectrometer. The FE of the various chemicals was calculated as follows:

$$FE_{GC} = \frac{4 * F * n_{GC}}{Q} \quad (7)$$

$$FE_{GX} = \frac{2 * F * n_{GX}}{Q} \quad (8)$$

$$FE_{\text{Glycine}} = \frac{12 * F * n_{\text{Glycine}}}{Q} \quad (9)$$

The glycine selectivity can be calculated as follows:

$$\text{Glycine selectivity} = \frac{n_{\text{Glycine}}}{n_{\text{Glycine}} + n_{\text{GX}} + n_{\text{GC}} + n_{\text{GAO}}} \times 100\% \quad (10)$$

where $n_{\text{Glycine}}/n_{\text{GX}}/n_{\text{GC}}/n_{\text{GAO}}$ is the mole of GC (glycolic acid)/GX (glyoxylic acid)/Glycine/GAO (glyoxylic acid oxime); F is the Faraday constant; Q is the total amount of charges passing the electrode.

Computational Details: Density functional theory as implemented in the Vienna Ab-initio Simulation Package (VASP) was employed to optimize geometry structures for glycine formation on Bi materials. The exchange-correlation interactions were described by the generalized gradient approximation (GGA) in the form of the Perdew-Burke-Ernzerhof functional (PBE). A cut-off energy of 450 eV for plain-wave basis sets was adopted and the convergence threshold was 10–5 eV, and 5×10^{-3} eV Å^{−1} for energy and force, respectively. The weak interaction was described by DFT+D3 method using empirical correction in Grimme's scheme. The vacuum space was set to be more than 15 Å, which was enough to avoid the interaction between periodical images. For Bi (012) surface, a three layer of 012 model was built. To calculate the lattice spacing, the following equation was used for R-3 m Bi crystal.

$$d_{hkl} = \frac{1}{\sqrt{\frac{4}{3} \frac{(h^2 + hk + k^2)}{a^2} + \left(\frac{l}{c}\right)^2}} \quad (11)$$

The reaction Gibbs free energy changes (ΔG) for each elementary step were based on the computational hydrogen electrode (CHE) model, which can be calculated by the following equation;

$$\Delta G = \Delta E + \Delta \text{ZPE} - T\Delta S \quad (12)$$

where ΔE is obtained directly from DFT calculations, ΔZPE is the change of zero-point energies (ZPE), T is the temperature of 298.15 K, and ΔS is the change in entropy of products and reactants. Standard ideal gas methods were employed to calculate ZPE and TS energy correction. For adsorbates, all 3N degrees of freedom were treated as frustrated harmonic vibration with the catalyst surface set to be fixed during the calculation.

Supporting Information

Supporting Information is available from the Wiley Online Library or from the author.

Acknowledgements

S.L. and G.W. contributed equally to this work. Q.Q. thanks to the financial support from the National Natural Science Foundation of China (Project No. 22305005), Science and Technology Youth Talent Program of Anhui Province (RCTJ202423), Natural Science Foundation of Anhui Province (2308085QB36) and Anhui Province University Scientific Research Project (2023AH050144). L.D. thanks the support from the National Natural Science Foundation of China (22202059). W.Z. thanks the support from the National Natural Science Foundation of China (Project No. 22405283).

Conflict of Interest

The authors declare no conflict of interest.

Data Availability Statement

The data that support the findings of this study are available in the supplementary material of this article.

Keywords

amino acid synthesis, C–N coupling, lattice engineering, NO₃[−] reduction

Received: January 13, 2025

Revised: March 16, 2025

Published online: April 3, 2025

- [1] a) Y.-P. Xue, C.-H. Cao, Y.-G. Zheng, *Chem. Soc. Rev.* **2018**, 47, 1516; b) J. F. Hyslop, S. L. Lovelock, P. W. Sutton, K. K. Brown, A. J. B. Watson, G. D. Roiban, *Angew. Chem., Int. Ed.* **2018**, 57, 13821.
- [2] J. Wang, X. Liu, X. Feng, *Chem. Rev.* **2011**, 111, 6947.
- [3] J. Wu, L. Xu, Z. Kong, K. Gu, Y. Lu, X. Wu, Y. Zou, S. Wang, *Angew. Chem., Int. Ed.* **2023**, 62, 202311196.
- [4] a) L. Li, C. Wan, S. Wang, X. Li, Y. Sun, Y. Xie, *Nano Lett.* **2024**, 24, 2392; b) J. Xian, S. Li, H. Su, P. Liao, S. Wang, Y. Zhang, W. Yang, J. Yang, Y. Sun, Y. Jia, Q. Liu, Q. Liu, G. Li, *Angew. Chem., Int. Ed.* **2023**, 62, 202304007; c) J. Xian, S. Li, H. Su, P. Liao, S. Wang, R. Xiang, Y. Zhang, Q. Liu, G. Li, *Angew. Chem., Int. Ed.* **2023**, 62, 202306726; d) Y. Wu, Z. Jiang, Z. Lin, Y. Liang, H. Wang, *Nat. Sustain.* **2021**, 4, 725; e) Z. Tao, C. L. Rooney, Y. Liang, H. Wang, *J. Am. Chem. Soc.* **2021**, 143, 19630.
- [5] a) Y. Cheng, P. Hou, H. Pan, H. Shi, P. Kang, *Appl. Catal., B* **2020**, 272, 118954; b) S. K. Mandal, P. C. Banerjee, *Process Biochem.* **2005**, 40, 1605.
- [6] a) G. Wu, W. Zhang, R. Yu, Y. Yang, J. Jiang, M. Sun, A. Du, W. He, L. Dai, X. Mao, Z. Chen, Q. Qin, *Angew. Chem., Int. Ed.* **2024**, 63, 202410251; b) G.-F. Chen, Y. Yuan, H. Jiang, S.-Y. Ren, L.-X. Ding, L. Ma, T. Wu, J. Lu, H. Wang, *Nat. Energy* **2020**, 5, 605.
- [7] Y. Cheng, S. Liu, J. Jiao, M. Zhou, Y. Wang, X. Xing, Z. Chen, X. Sun, Q. Zhu, Q. Qian, C. Wang, H. Liu, Z. Liu, X. Kang, B. Han, *J. Am. Chem. Soc.* **2024**, 146, 10084.
- [8] M. Li, Y. Wu, B.-H. Zhao, C. Cheng, J. Zhao, C. Liu, B. Zhang, *Nat. Catal.* **2023**, 6, 906.
- [9] a) S. Zuo, Z.-P. Wu, D. Xu, R. Ahmad, L. Zheng, J. Zhang, L. Zhao, W. Huang, H. Al Qahtani, Y. Han, L. Cavallo, H. Zhang, *Nat. Commun.* **2024**, 15, 9514; b) T. Liu, T. Xu, T. Li, Y. Jing, *J. Am. Chem. Soc.* **2024**, 146, 24133; c) J. Jiao, X. Kang, J. Yang, S. Jia, X. Chen, Y. Peng, C. Chen, X. Xing, Z. Chen, M. He, H. Wu, B. Han, *Angew. Chem., Int. Ed.* **2024**, 63, 202409563.
- [10] a) R. P. Janssonius, L. M. Reid, C. N. Virca, C. P. Berlinguette, *ACS Energy Lett.* **2019**, 4, 980; b) A. Khorshidi, J. Violet, J. Hashemi, A. A. Peterson, *Nat. Catal.* **2018**, 1, 263.
- [11] a) L. Wang, Z. Zeng, W. Gao, T. Maxson, D. Raciti, M. Giroux, X. Pan, C. Wang, J. Greeley, *Science* **2019**, 363, 870; b) G. Luo, Y. Wang, Y. Li, *Sci. Bull.* **2017**, 62, 1337.
- [12] J. K. N. B. Hammer, *Surf. Sci.* **1995**, 343, 211.
- [13] a) X. Yue, L. Cheng, F. Li, J. Fan, Q. Xiang, *Angew. Chem., Int. Ed.* **2022**, 61, 202208414; b) J. Hao, Z. Zhuang, J. Hao, K. Cao, Y. Hu, W. Wu, S. Lu, C. Wang, N. Zhang, D. Wang, M. Du, H. Zhu, *ACS Nano* **2022**, 16, 3251.
- [14] Z. Zhu, Y. Jiang, L. Xu, Q. An, T. T. T. Nga, J. Chen, Y. Fan, Q. Liu, C. L. Dong, S. Wang, Y. Zou, *Adv. Mater.* **2025**, 37, 2409864.
- [15] a) J. Feng, L. Wu, S. Liu, L. Xu, X. Song, L. Zhang, Q. Zhu, X. Kang, X. Sun, B. Han, *J. Am. Chem. Soc.* **2023**, 145, 9857; b) T. Kim, R. E. Kumar, J. A. Brock, E. E. Fullerton, D. P. Fenning, *ACS Catal.* **2021**, 11, 6662; c) C. Yang, H. Shen, A. Guan, J. Liu, T. Li, Y. Ji, A. M. Al-Enizi, L. Zhang, L. Qian, G. Zheng, *J. Colloid Interface Sci.* **2020**, 570, 375; d) J. Monzó, Y. Malewski, R. Kortlever, F. J. Vidal-Iglesias, J. Solla-Gullón, M. T. M. Koper, P. Rodriguez, *J. Mater. Chem.* **2015**, 3, 23690.
- [16] X. Kong, J. Ni, Z. Song, Z. Yang, J. Zheng, Z. Xu, L. Qin, H. Li, Z. Geng, J. Zeng, *Nat. Sustainability* **2024**, 7, 652.

- [17] a) M. Wang, Y. Gu, J. Li, H. Wang, M. Zhu, J. Liang, Z. Tie, J. Ma, Z. Jin, *Nano Energy* **2024**, 126, 109659; b) J. Li, T. Xiang, X. Liu, M. N. Ghazzal, Z. Q. Liu, *Angew. Chem., Int. Ed.* **2024**, 63, 202407287.
- [18] B. Ávila-Bolívar, M. L. Luna, F. Yang, A. Yoon, V. Montiel, J. Solla-Gullón, S. W. Chee, B. R. Cuenya, *ACS Appl. Mater. Interfaces* **2024**, 16, 11552.
- [19] S. Li, G. Wu, J. Mao, A. Chen, X. Liu, J. Zeng, Y. Wei, J. Wang, H. Zhu, J. Xia, X. Wang, G. Li, Y. Song, X. Dong, W. Wei, W. Chen, *Angew. Chem., Int. Ed.* **2024**, 63, 202407612.
- [20] J. Chen, T. Mao, J. Wang, J. Wang, S. Wang, H. Jin, *Angew. Chem., Int. Ed.* **2024**, 63, 202408849.
- [21] X. Cao, Y. Tian, J. Ma, W. Guo, W. Cai, J. Zhang, *Adv. Mater.* **2023**, 36, 202309648.
- [22] N. Li, C. Pan, G. Lu, H. Pan, Y. Han, K. Wang, P. Jin, Q. Liu, J. Jiang, *Adv. Mater.* **2023**, 36, 2311023.
- [23] W. Chen, C. Xie, Y. Wang, Y. Zou, C.-L. Dong, Y.-C. Huang, Z. Xiao, Z. Wei, S. Du, C. Chen, B. Zhou, J. Ma, S. Wang, *Chem* **2020**, 6, 2974.
- [24] Z. Fan, C. Cao, X. Yang, W. Yuan, F. Qin, Y. Hu, X. Sun, G. Liu, Y. Tian, L. Xu, *Angew. Chem., Int. Ed.* **2024**, 63, 202410356.
- [25] a) S. Jia, X. Tan, L. Wu, X. Ma, L. Zhang, J. Feng, L. Xu, X. Song, Q. Zhu, X. Kang, X. Sun, B. Han, *Chem. Sci.* **2023**, 14, 13198; b) Y. Yao, S. Zhu, H. Wang, H. Li, M. Shao, *J. Am. Chem. Soc.* **2018**, 140, 1496.
- [26] K. Fan, W. Xie, J. Li, Y. Sun, P. Xu, Y. Tang, Z. Li, M. Shao, *Nat. Commun.* **2022**, 13, 7598.
- [27] a) Y. Wu, J. Zhao, C. Wang, T. Li, B.-H. Zhao, Z. Song, C. Liu, B. Zhang, *Nat. Commun.* **2023**, 14, 3057; b) T. Zhang, T. He, C. Yan, X. Gao, J. Ma, H. Li, *Anal. Methods* **2018**, 10, 5817.